

Evaluation of thrust measurement techniques for dielectric barrier discharge actuators

Ryan Durscher · Subrata Roy

Received: 12 August 2011 / Revised: 25 June 2012 / Accepted: 26 June 2012 / Published online: 18 July 2012
© Springer-Verlag 2012

Abstract Despite its popularity in the recent literature, plasma actuators lack a consistent study to identify limitations, and remedy thereof, of various thrust measurement techniques. This paper focuses on comparing two different experimental techniques commonly used to measure the global, plasma-induced thrust. A force balance is used to make a direct measurement of the thrust produced, which is then compared with a control volume analysis on data obtained through particle image velocimetry. The local velocity measured by particle image velocimetry is also validated with a fine-tip pressure probe. For the direct thrust measurements, the effect of varying the actuator plate length upon which the induced flow acts is investigated. The results from these tests show that the length of the actuator plate is most influential at higher voltages with the measured thrust increasing as much as 20 % for a six times reduction in the length of the plate. For the indirect thrust measurement, the influence of the control volume size is analyzed. When the two methods are compared against each other, good agreement is found when the control volume size has a sufficient downstream extent. Also, the discharge length is optically measured using visible light emission. A linear correlation is found between the discharge length and the thrust measurements for the actuator configurations studied. Finally, the energy conversion efficiency curve for a representative actuator is also presented.

1 Introduction

The dielectric barrier discharge (DBD) plasma actuator, in general, consists of an asymmetric electrode arrangement (one exposed and one encapsulated) separated by a dielectric medium. The application of an alternating, high-voltage signal results in a surface-mode discharge along the dielectric. At (or near) atmospheric pressures, the discharge is comprised of micro-discharges which form discrete channels between the electrode and dielectric surface (Gibalov and Pietsch 2000; Kogelschatz 2003; Xu 2001). The expansion of the discharge along the dielectric surface results in a charge deposition, which in turn reduces the local electric field and extinguishes the micro-discharge. Collectively, the discharge is completely extinguished twice per period as evident by the light emission and discharge current (Enloe et al. 2004). As the ionized particles within the micro-discharges propagate along the dielectric surface, momentum is transferred to the surrounding neutral particles through a poorly understood collisional mechanism. Macroscopically, however, the net separated space charge within the plasma interacts with the electric field resulting in an electro-hydrodynamic body force acting on the working gas resulting in an acceleration of the fluid. By virtue of Newton's third law, an equal and opposite force is imparted to the actuator. Experiments have shown this momentum exchange to be cyclic with the magnitude of the force varying depending on the polarity of the exposed electrode (Debien et al. 2012, Enloe et al. 2008b; Enloe et al. 2009; Font et al. 2011).

The plasma actuator has been used as a flow control mechanism in various aerodynamic applications such as turbines blades (Ramakumar and Jacob 2005; Rizzetta and Visbal 2008), landing gears (Thomas et al. 2005), airfoils (Little et al. 2010; Post and Corke 2004), turbulent jets

R. Durscher · S. Roy (✉)
Applied Physics Research Group, Mechanical and Aerospace
Engineering Department, University of Florida, Gainesville,
FL 32611-6300, USA
e-mail: roy@ufl.edu

(Labergue et al. 2007), and an assortment of conical flows (e.g. flat plate boundary layers (Gibson et al. 2012; Grundmann and Tropea 2009; Roth et al. 2000; Schatzman and Thomas 2010), cylinder vortex shedding (Jukes and Choi 2009; Thomas et al. 2008), etc.). In order to improve the fluidic authority of the actuators, numerous parametric studies have been undertaken which have focused on various aspects (e.g. applied voltage/frequency, dielectric material, electrode arrangement) of the actuator (Abe et al. 2008; Borghi et al. 2008; Corke et al. 2007; Forte et al. 2007; Hoskinson and Hershkowitz 2010; Hoskinson et al. 2008; Jolibois and Moreau 2009; Roth and Dai 2006; Thomas et al. 2009). Characterizing the resulting induced thrust is therefore pivotal for understanding the influence of various control parameters in improving the actuator authority.

Several methods have been employed for measuring the plasma-induced thrust. Typically, a simplified approach is used to either measure the net thrust directly using a high resolution (\sim mg) force balance or calculate it indirectly based on the velocity field extracted using techniques such as Pitot probes, particle image velocimetry (PIV), and laser Doppler velocimetry (LDV). Specifically, the latter approach relies on a control volume analysis of the measured flow field to determine the net thrust produced (Baughn et al. 2006; Hoskinson et al. 2008; Kotsonis et al. 2011; Kriegseis 2011a; Debien et al. 2012). Recently, more complicated methods have also been investigated that resolves the plasma body force spatially by applying the Navier–Stokes momentum equations to PIV data (Kotsonis et al. 2011). However, a basic study aimed at the limitations of the simplified direct or indirect measurements is lacking. For example, the near wall flow as a result of actuation gives rise to a self-induced drag (Font et al. 2010), for which the plate size would likely have a significant impact on the measured thrust. The plate size, however, is not typically reported in the literature. Also, how does the calculated thrust vary with the size of control volume, and how does it compare with the direct measurement? In literature, a comparison between the two methods is often met with mixed results. Hoskinson et al. (2008) reported a factor of two difference in the calculated thrust between the two techniques (attributed to simplifications made), while Kotsonis et al. (2011) showed a reasonable agreement between the two methods.

This paper focuses on characterizing some limitations of the aforementioned direct and control volume inferred experimental techniques used to measure the net, induced thrust for a basic single dielectric barrier discharge (SDBD) actuator. In particular, the influence of the plate size on the direct thrust measurement is investigated. Similarly, the thrust is indirectly determined from a control volume analysis of the flow field obtained through PIV. Here, the

influence of the control volume size on the calculated thrust is analyzed by comparing with the plate size-independent direct thrust data. Also, the discharge length is optically measured using visible light emission. A functional relationship between the measured discharge length and the measured thrust is studied. The local velocity measured by the PIV technique is also validated with Pitot tube measurements at different locations. The paper is organized in the following manner. Section 2 describes the experimental setup for the tests conducted. This includes a discussion of the direct thrust measuring arrangement, PIV details, and the control volume analysis. Section 3 presents the results for the aforementioned investigations, while conclusions are drawn in Sect. 4.

2 Experimental arrangement

2.1 Plasma actuator design and discharge generation

A cross-sectional schematic of the DBD plasma actuator used in these experiments is shown in Fig. 1a. The actuator

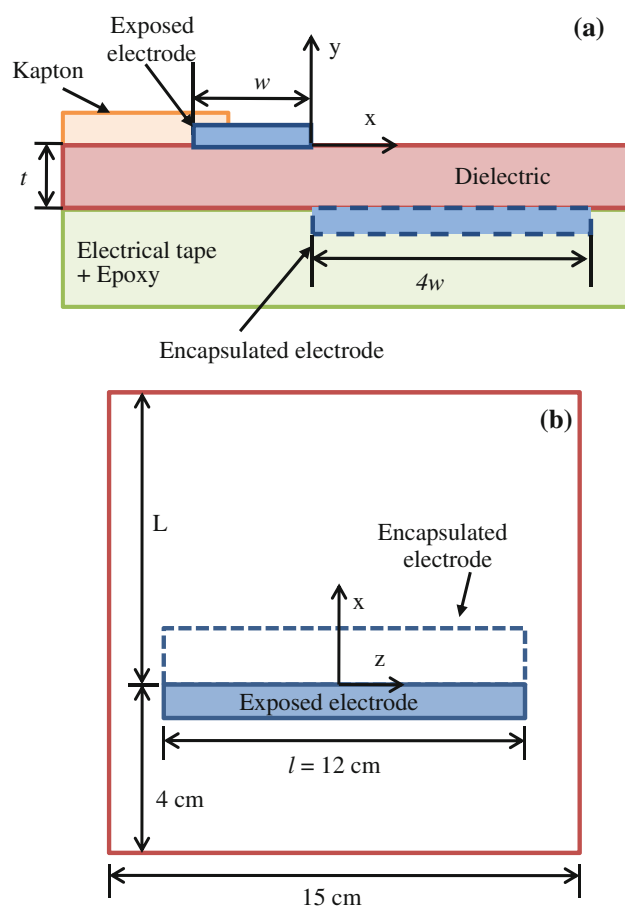


Fig. 1 Schematic of DBD plasma actuator: **a** side view and **b** top view (not drawn to scale)

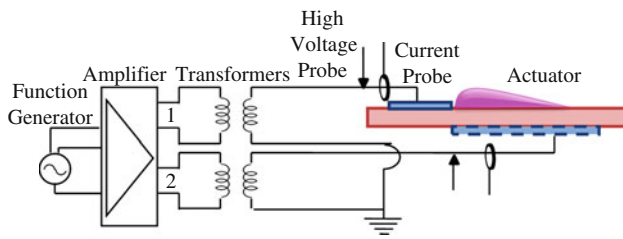


Fig. 2 Circuit schematic used to generate a DBD plasma discharge

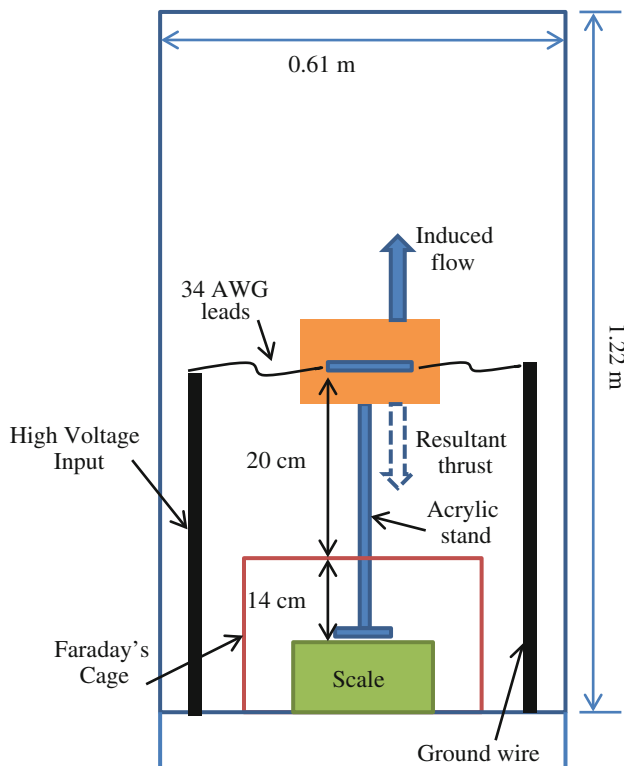


Fig. 3 Experimental setup schematic for direct force measurement

consists of two thin (70 μm) copper electrodes placed asymmetrically on either side of the dielectric material with no horizontal gap between the two electrodes. The dielectric in this case was a 3-mm-thick (t) sheet of acrylic which has a nominal relative dielectric constant of 3. The width, w , of the upper electrode was 0.5 cm while the lower electrode's width is 2 cm. Both electrodes have a length, l , of 12 cm. Three layers of vinyl electrical tape (178- μm thick) covered the encapsulated electrode to avert an unwanted discharge on the lower surface. Similarly, an 84- μm -thick piece of Kapton was placed on the opposite side of the exposed electrode preventing the occurrence of a discharge. The actuator depicted in Fig. 1b shows the dimensions of the dielectric used in the actuator plate length tests, where the effect on the thrust was investigated by shortening the actuator's plate length, L .

In order to ionize the surrounding air, the exposed and encapsulated electrodes were each supplied with high-voltage signals that were 180° out of phase. A congruent powering scheme has previously been used by Thomas et al. (2009). The sinusoidal input signals were generated using an arbitrary waveform generator (Tektronix AFG3022B). These signals were further amplified by a dual output audio amplifier (QSC RMX 2450) which was then stepped up using high-voltage transformers (Corona Magnetics, Inc. CMI 5523) (Fig. 2). Actuators were tested with total voltages ranging from 14 to 28 kVpp at two distinct frequencies 7 and 14 kHz.

The voltage and current supplied to the actuators were monitored using high-voltage (Tektronix P6015A) and current probes (Pearson Electronic 2100). In order to calculate the delivered power, the voltage and current waveforms were captured using a digitizing oscilloscope (Tektronix DPO3014). In a single acquisition, the oscilloscopes captured 1 million points for each waveform at a sampling rate of 250 MSa s^{-1} . For each input voltage, 10 acquisitions were recorded. This corresponds to 280 and 560 periods over which the calculated power is averaged for 7 and 14 kHz waveforms, respectively. The total power, P , delivered to the plasma actuator was considered to be a linear superposition of the power supplied to each electrode. The average real power was numerically calculated by multiplying the instantaneous voltage, V_i , by the instantaneous current, I_i , and then summing and dividing by the total number of samples, N . The indices 1 and 2 in Eq. 1 correspond to the respective circuit branches in Fig. 2.

$$P = \frac{1}{N} \left(\sum_{i=1}^N V_{1,i} I_{1,i} + \sum_{i=1}^N V_{2,i} I_{2,i} \right) \quad (1)$$

2.2 Direct thrust measurements

Direct thrust measurements were obtained using an Ohaus precision balance (Adventurer™ Pro AV313C). The actuators were mounted to the scale by an acrylic stand which protruded through a small opening in a Faraday's cage (Fig. 3). The cage was constructed using aluminum (3.18-mm thick) and was used to shield the balance from any electromagnetic interference due to the high electric fields required to generate the plasma discharge. To prevent ambient room currents from influencing the sensitive scale (of resolution 1 mg), the entire setup was housed in a large quiescent chamber with dimensions $0.61 \times 0.61 \times 1.22$ m (width \times depth \times height). Thin insulated wire (34 AWG) was used to connect the high-voltage input leads to the actuator in order to limit the rigidity of the wire from influencing the reading. For each input voltage, 15

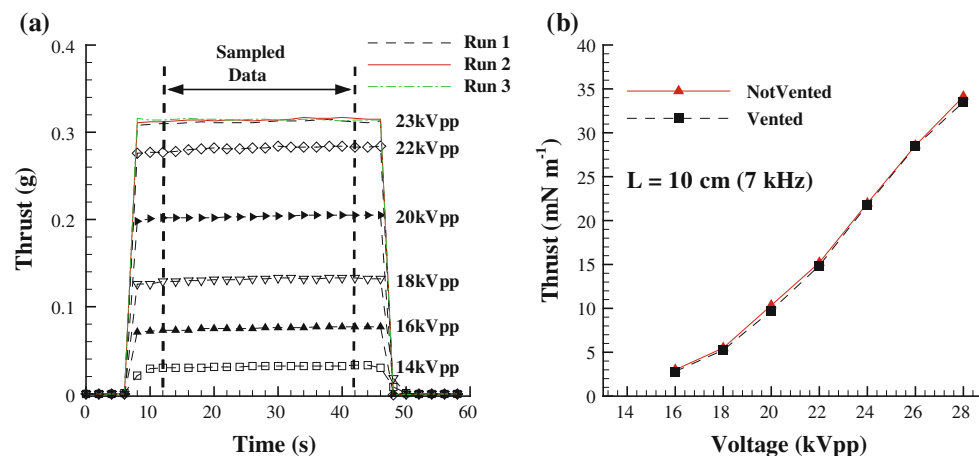


Fig. 4 **a** Example readouts from the balance showing the stability and repeatability of the direct thrust measurement (14 kHz). **b** Effect of a vented versus unvented chamber on the induced thrust (7 kHz). The plate length (L) was 10 cm for both plots

measurements were recorded from the scale over a 30-s span once an initial stable reading was reached. An example output from the balance is shown in Fig. 4a for various voltages. The maximum uncertainty associated with a given measurement is estimated to be within 4 % (to 95 % confidence), based on repeated measurements (at a constant voltage) and the scale's inherent uncertainty. Furthermore, the error in the thrust measurement due to the scale's cross-axis sensitivity was investigated and found to be negligible. This was determined by orienting the actuator on the mass balance to measure the z-component of the force (referring to Fig. 1). In such an arrangement, the scale would be affected by both x and y components in the cross-axis direction. Given that the z-component should be zero for a linear actuator, a registered thrust reading by the balance should presumably be a result of its sensitivity to cross-axis forces. No thrust was measured as the balance read zero over the entire range of input voltages.

Furthermore, the chamber in which the scale is housed is only slightly vented to prevent potentially dangerous amounts of ozone from continuously spreading into the laboratory. As a consequence, one could argue that for particularly long runs of the actuator that the air chemistry inside of the chamber is being modified. To test this argument, two tests were carried out over a range on input voltages. In one case, the 0.74 m² door to the chamber was closed during testing, while it was left wide open in the other. The measured thrust from these tests is shown in Fig. 4b, where “not vented” and “vented” correspond to the door being closed and open, respectively. As evident from the figure, the resultant thrust was nearly identical regardless of ventilation. This result would likely change if the volume of the quiescent chamber was reduced, though the results seem indifferent for the current experimental setup.

3 Control volume analysis

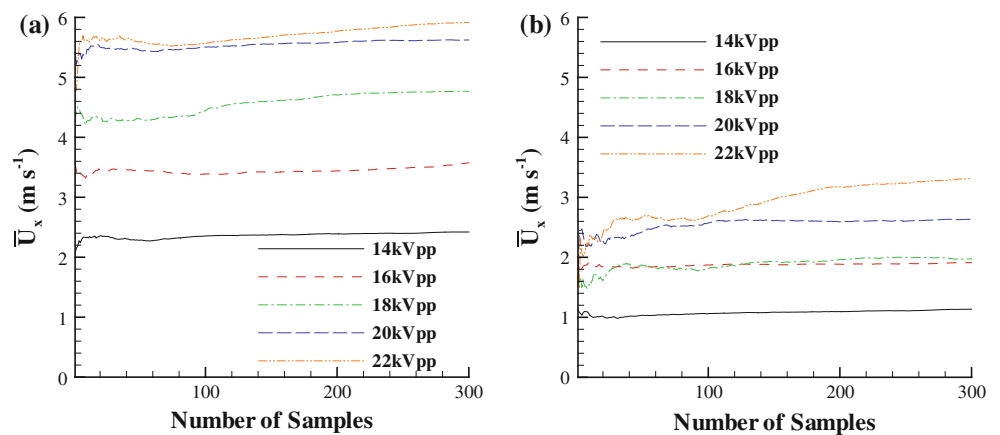
3.1 Flow field measurements

Two-component PIV was used to generate time-averaged, spatially resolved data of the induced flow due to the plasma actuation. These averaged vector fields were then used for the control volume analysis. The plasma actuator geometry is similar to that described previously (Fig. 1); however, the dielectric plate upon which the actuator was built was much larger. The dimensions of the plate are 30 cm × 30 cm with the electrodes placed in the center. The actuator was set up in the same quiescent chamber as described above.

A Nd:YAG, dual cavity pulsed 532-nm laser (New Wave Research Solo PIV II 30) was used to generate a light sheet along the centerline of the actuator normal to the dielectric surface. This illuminated the vaporized Ondina oil used to seed the chamber (see Sect. 7). Adjustable focal length optics allowed for fine adjustments to the waist of the laser sheet, which had an estimated thickness of 1 mm. The time separation (dt) between laser pulses was adjusted accordingly depending on the induced flow velocity. In general, the dt was set to maintain a maximum particle displacement of 5–7 pixels, with the value ranging from 48 to 22 μ s (voltage/velocity dependant). LaVision's ImagerProX 4 M (2,048 × 2,048 pixels) camera fitted with a 105-mm lens was used to capture the PIV images. The field of view for each image was approximately 48 mm × 48 mm (x, y).

LaVision's DaVis 7.2 PIV software package was used to calibrate, capture, pre-process, process, and post-process the PIV images. Image calibration was performed with a 40 mm × 40 mm, two-tiered calibration plate. In processing the PIV data, the local average intensity was

Fig. 5 Convergence plot for the x -component of velocity (\bar{U}_x) for two locations in the flow field (14 kHz driving frequency). **a** Point $(x, y) = (5, 0.5)$ mm and **b** $(x, y) = (35, 1.5)$ mm



subtracted from the raw images in order to increase the relative contrast between the particles and the background. Furthermore, a local particle intensity correction was applied in which the particle intensities are normalized over a window of 4 pixels, allowing smaller particles to contribute more effectively in the correlation. Having masked the surface of the actuator, each image pair was then subjected to a cross-correlation multi-grid procedure. The correlation process consisted of an initial pass with a 32×32 pixel² interrogation window with a 50 % overlap, followed by two refining passes with 16×16 pixel² windows again with 50 % overlaps. For the initial pass, a 1:1 Gaussian weight was applied to the integration windows, while a 2:1 was applied on the refining passes. This resulted in a resolution of 5.26 vectors per mm. Outliers were detected and removed using a recursive spatial outlier detection (Westerweel 1994) in between multi-grid passes as well as on the final vector field.

For each input voltage, 300 image pairs were taken at a repetition rate of 7.2 Hz. Typical convergence plots of the mean tangential velocity component (\bar{U}_x) are shown in Fig. 5a and b for two locations in the velocity field. The first point, (5, 0.5) mm, is representative of the high velocity region near the discharge (Fig. 5a), while the second position, (35, 1.5), is within the fully developed wall jet (Fig. 5b). After ~ 200 samples, the average values begin to converge to a constant value for both points. The relative statistical uncertainty ζ for these two points is shown in Fig. 6 as calculated from

$$\zeta = \frac{t_{N-1,95\%} \bar{\sigma}_x}{\bar{U}_x} \quad (2)$$

where $t_{N-1,95\%}$ is the t estimator ($N - 1$ degrees of freedom, 95 % confidence interval), $\bar{\sigma}_x$ is the standard deviation of the mean velocity, and \bar{U}_x is the mean velocity (x -component). The results indicate a maximum relative error of ~ 4 % in the velocity measurements.

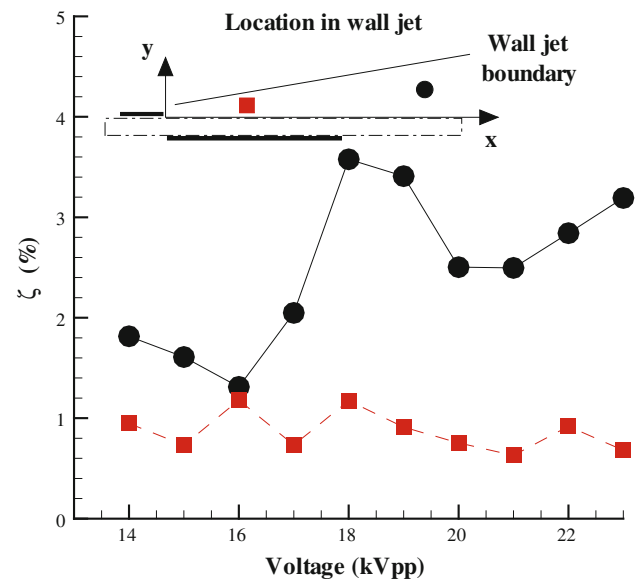


Fig. 6 Relative statistical uncertainty as a function of voltage and position for the velocity vector field (14 kHz driving frequency). Red squares correspond to point $(x, y) = (5, 0.5)$ mm while black circles represent $(x, y) = (35, 1.5)$ mm

3.1.1 PIV seeding

For the experiments outlined in this text, Ondina oil was used as the seeding particles. The oil was vaporized using a TSI atomizer (Model 9302) which, when pressurized at 25 psi, produces a droplet with a mean diameter of $\sim 0.8 \mu\text{m}$ (TSI 2000). Assuming a characteristic velocity of 5 m s^{-1} , a reference length of 1 mm, and Stokesian drag, the Stokes number (St) as defined by Adrian and Westerweel (2011) is 7.8×10^{-3} (or $St \ll 1$), indicating a reasonable fluidic response from the particles.

For plasma actuation, however, consideration of the electrodynamic influence on the particles is also warranted due to the presence of the large electric fields required to initiate the discharge. In doing so, the PIV images may be

broken into two regions: (1) the discharge volume itself and (2) the far-field away from the vicinity of the discharge. Within the discharge volume, a charging of the particle could result in a combination of fluidic and Coulombic forces influencing the particle's path. In the far-field, however, the dominant electrodynamic effect would likely be a dielectrophoretic force due to polarization of the particle. This is a topic which certainly remains an open area for future exploration as an electrodynamic influence on the seeding particles could potentially alter the accuracy of the velocity measurement and consequently the inferred thrust. Here, however, we will rely on a comparison of the vector field with and without seeding particles.

To investigate any potential electrodynamic effects on the seeding particles, the PIV velocity profiles were compared against measurements obtained using a Pitot (pressure) probe. The probe used was a United Sensor Corp. stainless steel “boundary layer probe” (Model BR-.025-12-C-11-.120) having an inner and outer diameter of 0.4318 and 0.635 mm, respectively. The design of the probe's tip, however, is flattened (the diameter is reduced by half), which significantly reduces its presence in the wall normal direction. Positioning of the probe was controlled using a two-axis traverse (Velmex MN10-0150-M02-21) with a minimum step size of 5 μm . The pressure measurements were made using a Furness Controls FCO332 differential manometer calibrated to ± 25 Pa with a ± 10 V output. Each data point represents the average of 800 voltage readings recorded at a sampling rate of 20 Hz using a National Instruments data acquisition module (PCI-6133). The differential pressure, ΔP , measurements were converted to velocities using Eq. 3 where ρ is the air density. Here, the air density was taken as 1.184 kg m^{-3} which corresponds to a laboratory temperature of 25°C . An error analysis was carried out on the

obtained data which took into account the accuracy of the transducer ($\pm 0.5\%$ Pa), the accuracy of the voltage reading (± 5 mV), and the statistical uncertainty of the sampled set.

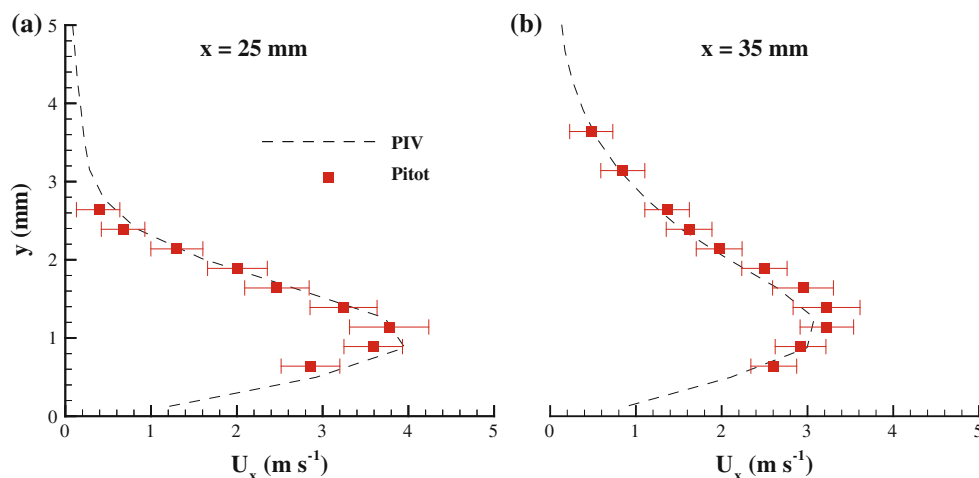
$$U_x = \sqrt{2\Delta P/\rho} \quad (3)$$

The use of a metallic probe limited the proximity in which a measurement may be made near the plasma. Furthermore, measurements near the dielectric surface were also prohibited as arcing was observed between the probe and the dielectric when the probe itself was in contact with surface. These problems were alleviated, however, by taking readings sufficiently far downstream (25 and 35 mm) and keeping the probe away the dielectric surface (>0.5 mm). As shown in Fig. 7, reasonably good agreement is seen between the two data sets both in terms of magnitude and shape giving some indication that electrodynamic effects may be negligible in the current experimental setup

3.1.2 Inferred thrust calculation

The rectangular control volume as depicted in Fig. 8 was applied to the time-averaged velocity field generated from the PIV measurements. The net thrust, T_x and T_y , produced by the actuator (normalized by the electrode length) is determined from the conservative form of the momentum equations assuming time independence (Eq. 4a, b). The net thrust produced would be the summation of the wall shear stress (F_s), pressure differential, and the plasma-induced body force (F_p), acting within and on the control volume. If the control volume boundaries are significantly removed from the bulk plasma, a constant pressure assumption may be made (Kotsonis et al. 2011), in which the net thrust in the x -

Fig. 7 Comparison between pitot measurements and PIV profiles taken at (a) 25 and (b) 35 mm downstream of the exposed electrode for an applied voltage of 20 kVpp at 14 kHz



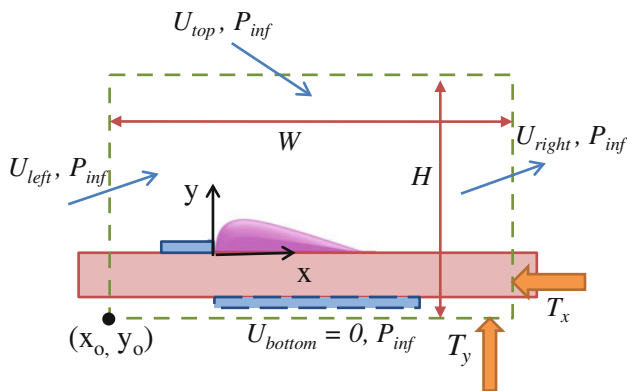


Fig. 8 Schematic of control volume used to calculate reaction forces induced by the plasma discharge

direction would be equal to $T_x = F_{x,p} - F_s$. In this analysis, however, we are interested in only the net thrust imparted to the dielectric. The control volume used is drawn accordingly to negate such distinctions. In particular, the boundaries of the volume extend below the dielectric surface where the velocity field is zero, to emphasis that the wall shear stress is not considered as a separate force. The thrust components are calculated from the velocity field as follows:

$$T_x = - \int_{y_0}^H \rho U_{x,\text{left}}^2 dy + \int_{x_0}^W \rho U_{x,\text{top}} U_{y,\text{top}} dx + \int_{y_0}^H \rho U_{x,\text{right}}^2 dy \quad (4a)$$

$$T_y = - \int_{y_0}^H \rho U_{y,\text{left}} U_{x,\text{left}} dy + \int_{x_0}^W \rho U_{y,\text{top}}^2 dx + \int_{y_0}^H \rho U_{y,\text{right}} U_{x,\text{right}} dy \quad (4b)$$

4 Results

4.1 Influence of the actuator plate length

In order to evaluate the effect of the actuator's plate length (L), shown in Fig. 1b, different plate lengths were tested. The same actuator was used throughout the experiments with the plate length, L , being reduced each time. Lengths corresponding to 15, 10, 5, and 2.5 cm were investigated over a range of voltages (14–28 kVpp). A plate length of 15 cm was chosen as to mimic the plate length of the actuator used in the control volume analysis. A limiting length of 2.5 cm was imposed to avoid the possibility of arcing around the dielectric substrate, since the encapsulated electrode itself is 2-cm wide. The lengths 10 and 5 cm were chosen arbitrarily as incremental lengths.

The results of this study, presented in Fig. 9, indicate that there is little variation in the resultant thrust regardless of the plate's length at lower input voltages. This trend does not hold, however, as the voltage increases. At the higher voltages investigated, an increase in thrust is observed, as the actuator's plate length is decreased. This increase is independent of the two frequencies investigated. At the maximum voltages tested, a difference of 5 and 7 mN/m was measured between plate lengths of 15 cm and 2.5 cm for 14 kHz and 7 kHz, respectively. This corresponds to a $\sim 20\%$ increase in the measured thrust for both cases (Fig. 10). Such a large discrepancy could prove problematic when trying to compare between different researchers' results if the plate length was not specified.

Because the viscous drag rapidly decreases in the downstream direction as the induced wall jet expands and dissipates, the difference in its integrated effect becomes less severe as the plate length is increased beyond a certain

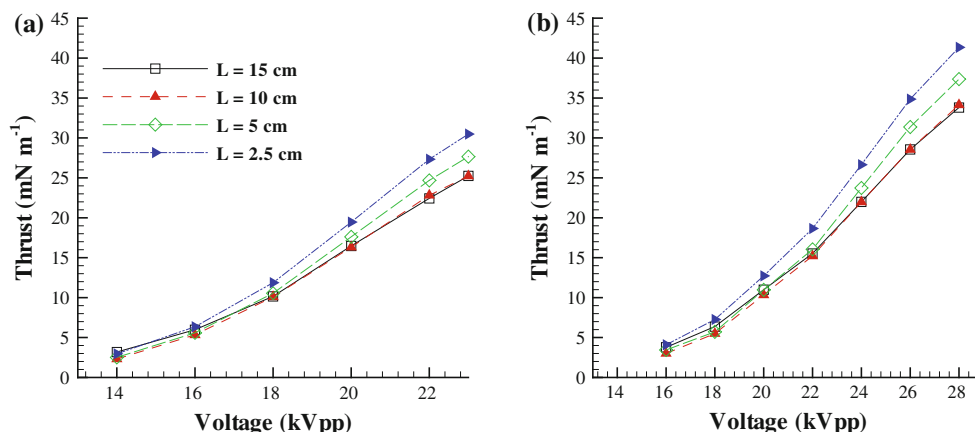


Fig. 9 Force measurements over a range of input voltages with varying actuator plate lengths: **a** 14 kHz and **b** 7 kHz

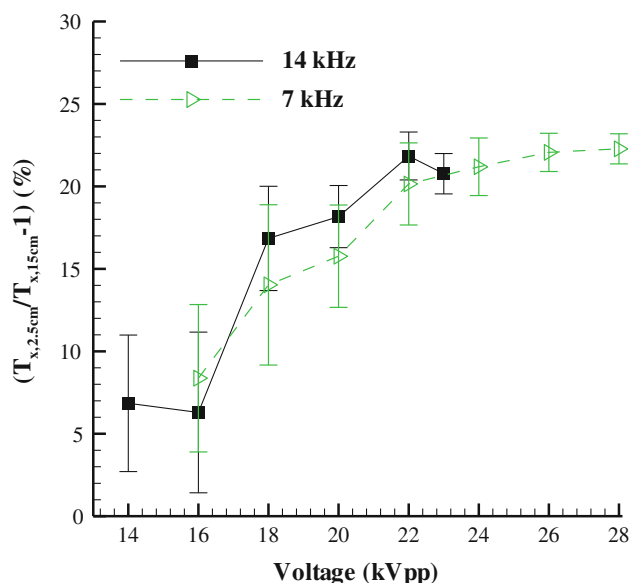


Fig. 10 Percentage increase in thrust between a plate length of 2.5 and 15 cm as a function of voltage

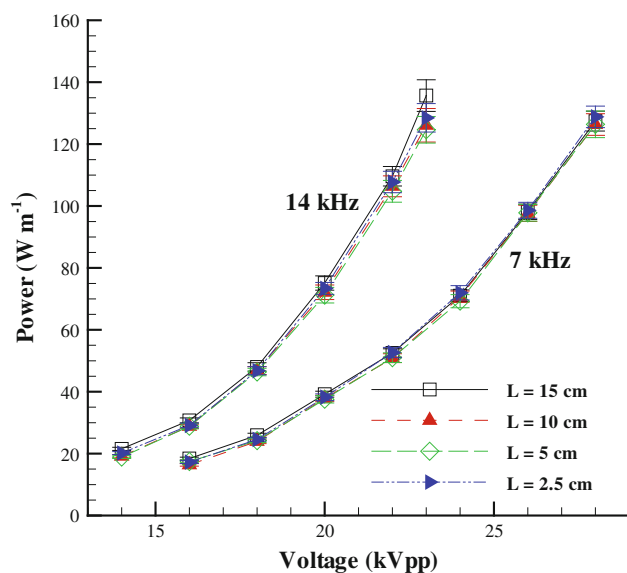


Fig. 11 Power dissipation as a function of voltage for different plate lengths

threshold (e.g. $L = 10$ cm). This results in nearly identical (plate-independent) thrust values for the longer plate lengths ($L = 10$ cm and 15 cm). For shorter plate lengths, however, the impact of the viscous drag overall would be significantly less than the longer plates, resulting in higher recoverable thrust readings. It is also plausible that a shortening of the dielectric plate affects the surface charge accumulation and thus the electric field and induced force on the fluid. A substantial surface charge has been shown to persist several centimeters downstream of an actuator (Opaitis et al. 2008; Enloe et al. 2008a, b). Regardless of the

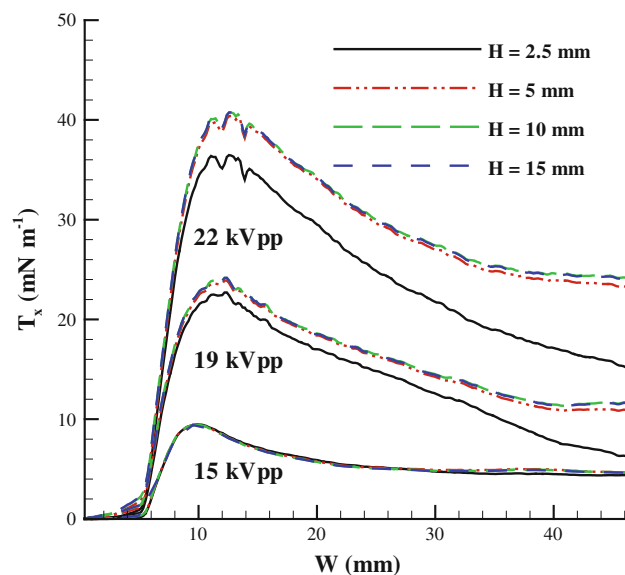


Fig. 12 Resultant tangential thrust component for a 15, 19, and 22 kVpp input voltage at 14 kHz as function of the width ($W = x - x_o$) for varying heights ($H = y - y_o$) of the control volume

exact mechanism, Fig. 11 verifies that the power consumption and thus power delivered to the plasma load remains constant regardless of the plate length, indicating a nominal constant body force is generated.

4.2 Control volume extracted forces

In order to extract the reaction thrusts on the control volume, the integrals on the right-hand side of Eq. 4a and b were numerically integrated in Matlab using the time-averaged PIV data. A composite trapezoidal rule was used for the integration scheme. It was found that the starting x -location, x_o , in the integrals had little influence on the resultant thrust calculated as long as it was chosen behind the edge of the exposed electrode (i.e. $x_o < x = 0$, referring to Fig. 8). The starting y -location, y_o , was chosen arbitrarily below the dielectric material such that $y_o < 0$ (Fig. 8). The starting locations used were -5.0 and -0.1 mm corresponding to x_o and y_o , respectively. Also, it is pertinent to note that a constant air density (ρ) is assumed. This assumption was also made by Hoskinson et al. (2008) based on prior experimental data from Enloe et al. (2006). In this prior work, it was estimated that the density fluctuations near the actuator were less than 2 % of ambient. Again, the air density was taken as 1.184 kg m^{-3} .

Figure 12 depicts typical plots of the inferred tangential thrust component, T_x , and how it varies with the width ($W = x - x_o$) and the height ($H = y - y_o$) of the control volume (referring to Fig. 8) for various voltages. The plot indicates that the thrust is independent of the control volume's height beyond a given point (10 mm for all cases

investigated). This point corresponds to the total encapsulation of the induced wall jet's "boundary layer". The boundary layer created by the jet increases with both applied voltage and downstream location. However, for the range of voltages investigated, the boundary layer was less than 10-mm thick for the given field of view. More important than the height of the control volume is its width, as Fig. 12 reveals. The calculated net thrust is highly dependent on the point at which the control volume ends. If the width is too small, the thrust may be grossly over-predicted as compared to a much wider control volume.

The tangential and normal thrust components are plotted in Fig. 13a and b, respectively, over the range of input voltages investigated. At each voltage, the thrust was extracted for five different control volume widths from data similar to Fig. 14. The vertical dashed lines in Fig. 14 correspond to control volume widths of 10, 20, 30, 40, and 45 mm. The height of the control volume chosen was 10 mm, which is a suitable choice for reasons previously discussed. Over the range of supplied voltages, the calculated tangential thrust shows a strong dependency on the width of the control volume. This dependency becomes more pronounced at higher voltages. The calculated thrusts do begin to plateau as the downstream extent of the control volume is increased. This is a result of the asymptotic

nature of the curves shown in Fig. 12. We note that the thrust does continually decrease as the downstream extent is increased due the perpetual addition of viscous drag. However, the rate of this decrease begins to slow as the wall jet expands and dissipates.

The normal thrust component deviates from this trend with its values remaining approximately constant as the width of the control volume is increased (Fig. 13b). The exception, however, to this observation is the smallest control volume plotted ($W = 10$ mm). Regardless, the magnitude of the normal component is significantly less than that of the tangential. The large disparity between the normal and tangential components is in line with other reports (Cheong et al. 2011).

4.3 Comparison between the two measurement methods

A comparison between the control volume analysis and the direct thrust measurement is shown in Fig. 15. Two different control volume widths ($W = 20$ and 40 mm) are presented, as well as the plate-independent direct thrust measurements ($L = 10$ cm). Results indicate that the measured and inferred thrusts are in good agreement over the entire voltage range for the wider ($W = 40$ mm)

Fig. 13 Forces calculated from a control volume analysis as a function of voltage for various widths ($W = x - x_o$) of the control volume (14 kHz): **a** tangential component of force (T_x) and **b** normal component of force (T_y)

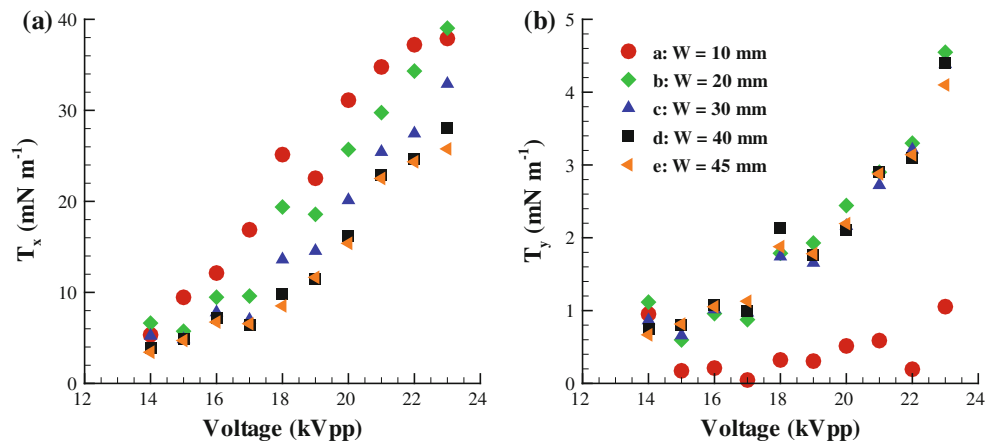
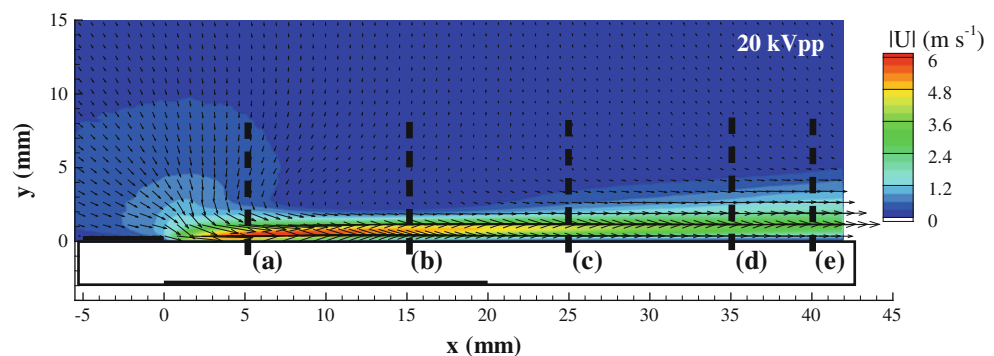


Fig. 14 Velocity magnitude contour for 20 kVpp input driven at 14 kHz. The dashed lines labeled (a) through (e) correspond to control volume widths ($W = x - x_o = x - (-5)$ mm) of 10, 20, 30, 40, and 45 mm, respectively



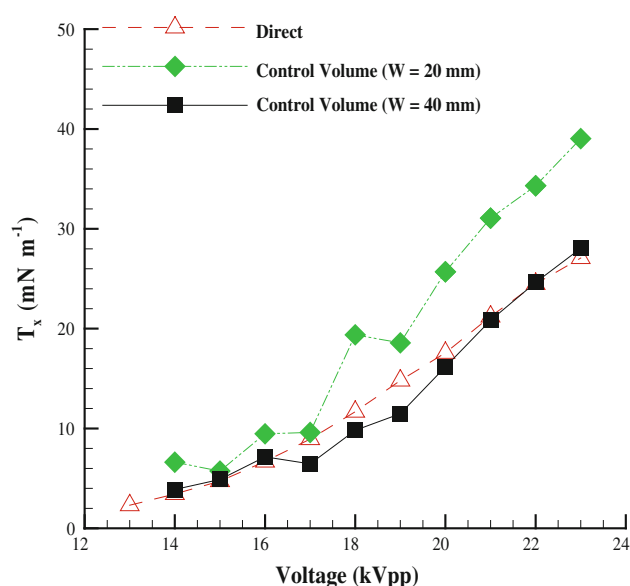


Fig. 15 Comparison between direct thrust measurements and those inferred from a control volume analysis. The driving frequency was 14 kHz

control volume. It is also evident that if the control volume is of insufficient size, the thrust may be over-predicted and eludes that there is a minimum length downstream of the actuator that the control volume needs to consider. That length, however, is directly tied to the applied voltage as there is a decent agreement for the smaller control volume width at lower input voltages. Based on these results, a downstream extension of ~ 35 mm is recommended.

Identifying the plate-independent direct thrust with a single parameter could be useful for practical purposes. A non-invasive parameter of choice, as suggested by Kriegseis et al. 2011b, is the plasma length (L_p) which results from the combination of geometric and electrical inputs. The plasma length was determined from photographs obtained using a Nikon D90 digital camera fitted with a 105-mm lens (8-s exposure, $f/7.1$). The color images were first converted to grayscale, then binarized using a

threshold value of 0.08. A tracing algorithm then mapped out the plasma, and an average length was determined. This value is plotted in Fig. 16a against the plate-independent direct thrust measurements for $L = 10$ cm presented in Fig. 15. A linear relationship was found between the direct thrust data ($T_{x,Direct}$) in mN m^{-1} and the plasma length (L_p) in mm.

$$T_{x,Direct} = 6.57L_p - 18.9 \quad (5a)$$

To determine the minimum threshold for the control volume size for reasonably predicting thrust, the same scaling metric (L_p) was studied. A linear relation of the form

$$x_{min} = 7.12L_p - 11.1 \quad (5b)$$

was obtained for the minimum control volume's downstream extent ($x_{min} = W_{min} + x_o$). This relation was found by matching the direct thrust data from Fig. 15 ($L = 10$ cm) with the PIV inferred thrust data, represented in Fig. 12, for given voltages. The difference between the inferred thrust using the minimum control volume extension and the direct measurements are provided in Fig. 16b on a percentage basis. As a comparison, the percentage difference in using a fixed control volume is also shown. In general (with exception of the lower voltages), using the minimum control volume extent yields better or similar results to that of the fixed width volume for $W = 40$ mm. Furthermore, the plot also emphasizes the over-prediction of the thrust when using a control volume of insufficient size (in this case $W = 20$ mm).

4.4 Energy conversion efficiency

The device characterization of an actuator tested in quiescent conditions is not complete without an understanding of its energy conversion efficiency, η , which is defined as (Zito et al. 2012) the ratio of thrust (T_x) and induced maximum velocity ($U_{x,max}$) to that of the delivered power (P):

Fig. 16 a Thrust as a function plasma length and **b** the percent difference between direct and control volume inferred forces using a fixed and scaled control volume

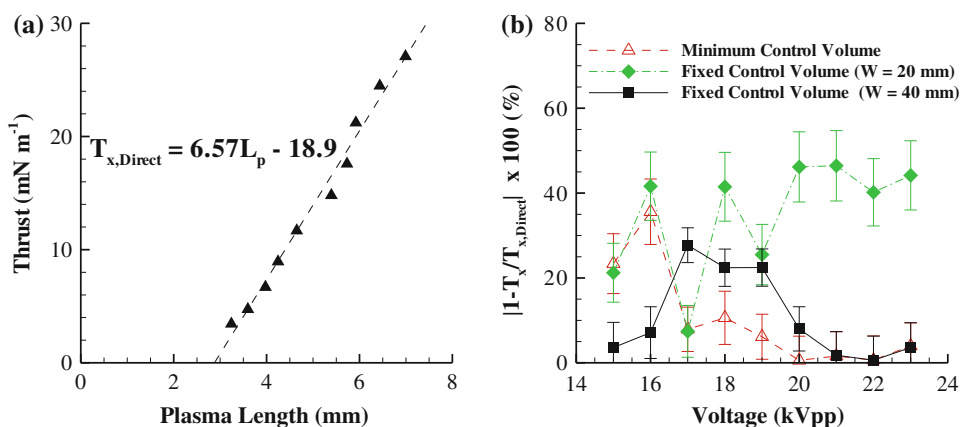
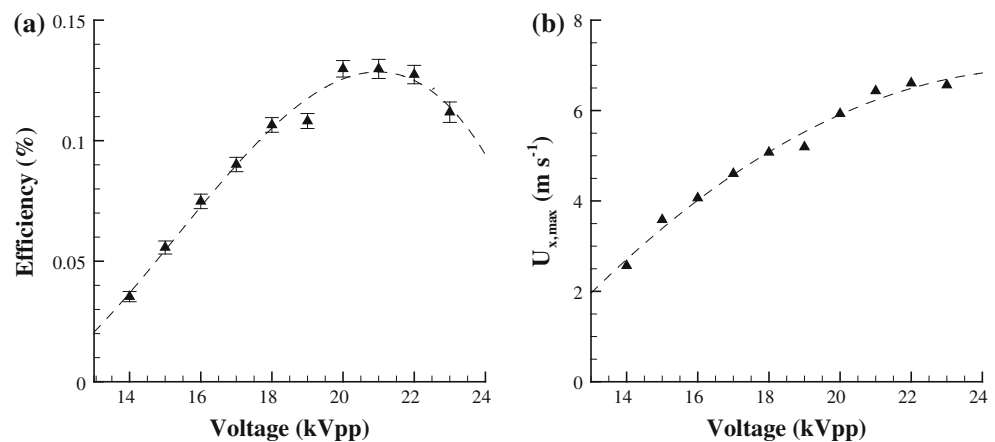


Fig. 17 **a** Energy conversion efficiency and **b** peak-induced velocity of a DBD actuator made from a 3-mm-thick acrylic plate operating at 14 kHz



$$\eta = \frac{T_x U_{x,\max}}{P} \quad (6)$$

The calculated efficiency for the actuator geometry used in this text for a driving frequency of 14 kHz is plotted as a function of the applied voltage in Fig. 17a, with the maximum velocity extracted from collected PIV data shown in Fig. 17b. While the efficiency of the DBD actuator is less than 0.15 %, the results show a peak efficiency region for the device. As the voltage is further increased, the induced velocity saturates and the efficiency drops implying more power loss in dielectric heating and/or streamer formation.

5 Conclusion

The effect of varying the plate length upon which the plasma-induced wall jet acted was investigated using a direct force balance. At the upper range of the voltages investigated, an increase in thrust was observed as the plate length was decreased. The thrust was nearly identical for 10- and 15-cm lengths, but an increase in thrust of 20 % was observed as the plate length was reduced to 2.5 cm (a four to six times reduction). Based on these findings, the plate's length is an important consideration when making comparisons with reported experimental data. PIV measurements were also made on a single DBD actuator at various voltages. These measurements provided time-averaged data sets of the induced flow field. The velocity fields were then subjected to a control volume analysis to infer the resultant thrusts acting on a rectangular volume. The results of the analysis indicated a strong dependency on the size of the considered volume with a particular emphasis on the width of it. When compared with the direct thrust measurements, the calculated tangential thrust agreed well regardless of the input voltage if the control volume extended far enough downstream. Also, the discharge length was optically measured using visible light

emission. A linear correlation was found between the plasma length and the measured thrust for the actuator configurations studied. A suitable control volume size was also recommended based on the plasma length. Finally, to complete the device characterization, the energy conversion efficiency curve for a representative actuator is also plotted.

Acknowledgments This work was sponsored in part under Air Force Office of Scientific Research Grants #FA9550-09-1-0372 and #FA9550-09-1-0615 monitored by Dr. Doug Smith and Charles Suchomel.

References

- Abe T, Takizawa Y, Sato S, Kimura N (2008) Experimental study for momentum transfer in a dielectric barrier discharge plasma actuator. *AIAA J* 46(9):2248–2256
- Adrian RJ, Westerweel J (2011) Particle image velocimetry. Cambridge University Press, Cambridge
- Baughn JW, Porter CO, Peterson BL, McLaughlin TE, Enloe CL, Font GI, Baird C (2006) Momentum transfer for an aerodynamic plasma actuator with an imposed boundary layer. In: 44th AIAA aerospace sciences meeting. AIAA 2006-168
- Borghi CA, Carraro MR, Cristofolini A, Neretti G (2008) Electrohydrodynamic interaction induced by a dielectric barrier discharge. *J Appl Phys* 103(6):063304
- Cheong M, Greig A, Gibson B, Arjomandi M (2011) An investigation into the effect of electric field on the performance of dielectric barrier discharge plasma actuators. *Exp Therm Fluid Sci* 35(8): 1600–1607
- Corke TC, Post ML, Orlov DM (2007) Sdbd plasma enhanced aerodynamics: concepts, optimization and applications. *Prog Aerosp Sci* 43(7–8):193–217
- Debien A, Benard N, David L, Moreau E (2012) Unsteady aspect of the electrohydrodynamic force produced by surface dielectric barrier discharge actuators. *Appl Phys Lett* 100(1):013901. doi: [10.1063/1.3674308](https://doi.org/10.1063/1.3674308)
- Enloe CL, McLaughlin TE, Vandyken RD, Kachner KD, Jumper EJ, Corke TC (2004) Mechanisms and responses of a single dielectric barrier plasma actuator: plasma morphology. *AIAA J* 42(3):589–594
- Enloe CL, McLaughlin TE, Font GI, Baughn JW (2006) Parameterization of temporal structure in the single-dielectric-barrier aerodynamic plasma actuator. *AIAA J* 44(6):1127–1136

- Enloe CL, Font GI, McLaughlin TE, Orlov DM (2008a) Surface potential and longitudinal electric field measurements in the aerodynamic plasma actuator. *AIAA J* 46(11):2730–2740
- Enloe CL, McHarg MG, McLaughlin TE (2008b) Time-correlated force production measurements of the dielectric barrier discharge plasma aerodynamic actuator. *J Appl Phys* 103(7):073302
- Enloe CL, McHarg MG, Font GI, McLaughlin TE (2009) Plasma-induced force and self-induced drag in the dielectric barrier discharge aerodynamic plasma actuator. In: 47th AIAA aerospace sciences meeting including the new horizons forum and aerospace exposition. AIAA 2009-1622
- Font GI, Enloe CL, McLaughlin TE (2010) Plasma volumetric effects on the force production of a plasma actuator. *AIAA J* 48(9):1869–1874. doi:[10.2514/1.51660](https://doi.org/10.2514/1.51660)
- Font GI, Enloe CL, Newcomb JY, Teague AL, Vasso AR, McLaughlin TE (2011) Effects of oxygen content on dielectric barrier discharge plasma actuator behavior. *AIAA J* 49(7):1366–1373. doi:[10.2514/1.55031](https://doi.org/10.2514/1.55031)
- Forte M, Jolibois J, Pons J, Moreau E, Touchard G, Cazalens M (2007) Optimization of a dielectric barrier discharge actuator by stationary and non-stationary measurements of the induced flow velocity: application to airflow control. *Exp Fluids* 43:917–928. doi:[10.1007/s00348-007-0362-7](https://doi.org/10.1007/s00348-007-0362-7)
- Gibalov VI, Pietsch GJ (2000) The development of dielectric barrier discharges in gas gaps and on surfaces. *J Phys D Appl Phys* 33(20):2618
- Gibson BA, Arjomandi M, Kelso RM (2012) The response of a flat plate boundary layer to an orthogonally arranged dielectric barrier discharge actuator. *J Phys D Appl Phys* 45(2):025202
- Grundmann Sven, Tropea Cameron (2009) Experimental damping of boundary-layer oscillations using dbd plasma actuators. *Int J Heat Fluid Flow* 30(3):394–402
- Hoskinson AR, Hershkowitz N (2010) Differences between dielectric barrier discharge plasma actuators with cylindrical and rectangular exposed electrodes. *J Phys D Appl Phys* 43(6):065205
- Hoskinson AR, Hershkowitz N, Ashpis DE (2008) Force measurements of single and double barrier dbd plasma actuators in quiescent air. *J Phys D Appl Phys* 41(24):245209
- Jolibois J, Moreau E (2009) Enhancement of the electromechanical performances of a single dielectric barrier discharge actuator. *Dielectr Electr Insulation IEEE Trans* 16(3):758–767
- Jukes TN, Choi K-S (2009) Long lasting modifications to vortex shedding using a short plasma excitation. *Phys Rev Lett* 102:254501
- Kogelschatz U (2003) Dielectric-barrier discharges: their history, discharge physics, and industrial applications. *Plasma Chem Plasma Process* 23:1–46. doi:[10.1023/A:1022470901385](https://doi.org/10.1023/A:1022470901385)
- Kotsonis M, Ghaemi S, Veldhuis L, Scarano F (2011) Measurement of the body force field of plasma actuators. *J Phys D Appl Phys* 44(4):045204
- Kriegseis J (2011a) Performance characterization and quantification of dielectric barrier discharge plasma actuators. Ph.D thesis, TU Darmstadt
- Kriegseis J, Grundmann S, Tropea C (2011b) Power consumption, discharge capacitance and light emission as measures for thrust production of dielectric barrier discharge plasma actuators. *J Appl Phys* 110(1):013305
- Labergue A, Moreau E, Zouzou N, Touchard G (2007) Separation control using plasma actuators: application to a free turbulent jet. *J Phys D Appl Phys* 40(3):674
- Little Jesse, Nishihara Munetake, Adamovich Igor, Samimy Mo (2010) High-lift airfoil trailing edge separation control using a single dielectric barrier discharge plasma actuator. *Exp Fluids* 48:521–537. doi:[10.1007/s00348-009-0755-x](https://doi.org/10.1007/s00348-009-0755-x)
- Opaits DF, Shneider MN, Miles RB, Likhanskii AV, Macheret SO (2008) Surface charge in dielectric barrier discharge plasma actuators. *Phys Plasmas* 15(7):073505
- Post ML, Corke TC (2004) Separation control on high angle of attack airfoil using plasma actuators. *AIAA J* 42(11):2177–2184
- Ramakumar K, Jacob JD (2005) Flow control and lift enhancement using plasma actuators. In: 35th AIAA fluid dynamics conference and exhibit. AIAA 2005-4635
- Rizzetta DonaldP, Visbal MiguelR (2008) Plasma-based flow-control strategies for transitional highly loaded low-pressure turbines. *J Fluids Eng* 130(4):041104
- Roth JR, Dai X (2006) Optimization of the aerodynamic plasma actuator as an electrohydrodynamic (ehd) electrical device. In: 44th AIAA aerospace sciences meeting and exhibit. AIAA 2006-1203
- Roth JR, Sherman DM, Wilkinson SP (2000) Electrohydrodynamic flow control with a glow-discharge surface plasma. *AIAA J* 38(7):1166–1172
- Schatzman DM, Thomas FO (2010) Turbulent boundary-layer separation control with single dielectric barrier discharge plasma actuators. *AIAA J* 48(8):1620–1634
- Thomas FO, Kozlov A, Corke TC (2005) Plasma actuators for landing gear noise reduction. In: 11th AIAA/CEAS aeroacoustics conference (26th AIAA Aeroacoustics Conference). AIAA 2005-3010
- Thomas FO, Kozlov A, Corke TC (2008) Plasma actuators for cylinder flow control and noise reduction. *AIAA J* 46(8):1921–1931
- Thomas F, Corke T, Iqbal M, Kozlov A, Schatzman D (2009) Optimization of dielectric barrier discharge plasma actuators for active aerodynamic flow control. *AIAA J* 47(9):2169–2178
- TSI (2000) Model 9302 atomizer, instruction manual. TSI Inc., St. Paul, MN
- Westerweel J (1994) Efficient detection of spurious vectors in particle image velocimetry data. *Exp Fluids* 16:236–247. doi:[10.1007/BF00206543](https://doi.org/10.1007/BF00206543)
- Xu X (2001) Dielectric barrier discharge—properties and applications. *Thin Solid Films* 390(1–2):237–242
- Zito J, Durscher R, Soni J, Roy S, Arnold D (2012) Flow and force inducement using micro size dielectric barrier discharge actuators. *Appl Phys Lett* 100:193502